Aust. J. Phys., 1985, 38, 449–69

Burgers Vectors in Secondary Grain Boundary Dislocation Structures for near Σ9, Σ27 and Σ81 Boundaries*

C. T. Forwood and L. M. Clarebrough

Division of Chemical Physics, CSIRO,
P.O. Box 160, Clayton, Vic. 3168.

Abstract

The Burgers vectors of secondary grain boundary dislocations, forming networks in near Σ9, Σ27a, Σ27b and Σ81a grain boundaries in polycrystalline specimens of a Cu +6 at.% Si alloy, have been determined using the technique of image matching, which involves a comparison of experimental and theoretical electron micrographs. In all cases, the Burgers vectors of the secondary grain boundary dislocations were found to be vectors of the DSC lattice corresponding to the appropriate CSL orientation. Further, in most cases, the Burgers vectors were found to be basis DSC vectors.

1. Introduction

The application of transmission electron microscopy to the study of the structure of high angle grain boundaries in polycrystalline metals and alloys has shown that such boundaries contain arrays of dislocations when the observed misorientations between neighbouring grains depart from exact coincident site lattice (CSL) orientations† (see e.g. Bollmann *et al.* 1972; Pumphrey 1975; Clark and Smith 1978; Forwood and Clarebrough 1983). These dislocations have commonly been identified with the secondary grain boundary dislocations (GBDs) in the model of a high angle boundary (Bollmann 1967) in which secondary GBDs accommodate the departure of the observed misorientation from an exact CSL orientation. In this model the Burgers vectors of the secondary GBDs are vectors of the DSC lattice,§ so that the displacements associated with them maintain the CSL relationship.

Although the dislocations observed in high angle boundaries have been commonly

* Dedicated to Dr A. McL. Mathieson on the occasion of his 65th birthday.

† Coincident site lattices occur at particular misorientations between neighbouring grains and consist of those lattice points which are coincident when the two misoriented lattices are allowed to interpenetrate. A particular CSL is specified by a parameter Σ, where 1/Σ of the lattice points are common to both lattices. If more than one CSL exists for a particular Σ value they are denoted a, b, c, etc. where a is given to the smallest angle of misorientation, b is the next smallest, etc. For CSLs with the same values of Σ and the angle of misorientation alphabetic, precedence is given to the CSL with the smallest sum of the squares of the indices of the rotation axis.

§ The DSC lattice is the coarsest lattice that contains all the lattice sites of both grains when they are misoriented at the CSL orientation.

0004-9506/85/030449$02.00

identified with the secondary GBDs of the theoretical model, there has only been one example of positive experimental identification of the Burgers vectors of secondary GBDs as DSC vectors from their diffraction contrast in electron microscope images, and this was for a near $\Sigma 9$ boundary in copper (Clarebrough and Forwood 1980*a*, 1980*b*). In that example, it was also shown that the arrays of secondary GBDs did accommodate the departure of the observed misorientation from the exact $\Sigma 9$ orientation. However, there is a need to see if the theoretical model verified for a near $\Sigma 9$ boundary applies, more generally to high angle boundaries with other Σ values. In the present paper the Burgers vectors of secondary GBDs in arrays in near $\Sigma 9$, $\Sigma 27$a, $\Sigma 27$b and $\Sigma 81$a boundaries are identified from their diffraction contrast and it is shown that in all cases the Burgers vectors involved are DSC vectors.

2. General Principles

The secondary GBD model for the structure of a general high angle grain boundary can be formulated as follows. If, for a general boundary, the misorientation between the grains is given by a rotation θ about an axis $\boldsymbol{R}$ and is close to a CSL orientation, corresponding to a rotation ω about an axis $\boldsymbol{P}$, then the small angular departure from the exact CSL will be given by a rotation ϕ about an axis $\boldsymbol{u}$, according to the matrix equation

$$(\boldsymbol{R}, \theta) = (\boldsymbol{u}, \phi) . (\boldsymbol{P}, \omega) . \tag{1}$$

The secondary GBDs required to accommodate the small misorientation $(\boldsymbol{u}, \phi)$ can be described by the equation given by Frank (1950),

$$\boldsymbol{B} = 2(\boldsymbol{x} \times \boldsymbol{u}) \sin \tfrac{1}{2}\phi , \tag{2}$$

where $\boldsymbol{B}$ is the net Burgers vector of the secondary GBDs intersected by any vector $\boldsymbol{x}$ lying in the plane of the boundary. In equation (2) $\boldsymbol{B}$ is linearly dependent on $\boldsymbol{x}$ and this can only be satisfied, for any vector $\boldsymbol{x}$ in the plane of the boundary, if the secondary GBDs occur in arrays where the GBDs in each array are parallel and equally spaced. It can also be seen from equation (2) that the net Burgers vector $\boldsymbol{B}$ must always lie in the plane normal to $\boldsymbol{u}$ and, in general, this will not be a simple low-index crystallographic plane. Thus, to satisfy this condition, the structure of the boundary must consist of at least three arrays of secondary GBDs with non-coplanar Burgers vectors. The Burgers vectors of secondary GBDs are vectors of the DSC lattice and these DSC vectors are specific to particular CSL orientations and crystal structures. They can be obtained from the $(\boldsymbol{P}, \omega)$ matrix in the manner described by Grimmer *et al.* (1974). However, in the present paper DSC vectors will be obtained by adopting a simpler procedure using the theorem of Grimmer (1974), which shows that the DSC lattice is reciprocal to the coincidence lattice of the two reciprocal lattices of the grains at the CSL orientation. The coincidence lattice of the two reciprocal lattices corresponds to those sets of planes which are crystallographically equivalent, with plane normals g_c, and which are continuous across the boundary. The three smallest non-coplanar g_c vectors can be obtained directly for cubic crystals from the rotation matrix $(\boldsymbol{P}, \omega)$.* If these are taken as the rows of a 3×3 matrix, then the basis vectors of the DSC lattice, corresponding to the CSL under consideration, are simply given by the columns of the inverse matrix. For example, in the case of an exact $\Sigma 3$ boundary in a f.c.c. bicrystal, where grain 2 is rotated clockwise by an angle ω of 60° with respect to grain 1 about an axis $\boldsymbol{P}$ parallel to [111] in both grains, then a direction with indices $[uvw]_1$ in grain 1 and $[u'v'w']_2$ in grain 2 are related by the equation

$$\begin{bmatrix} u \\ v \\ w \end{bmatrix}_1 = \frac{1}{3} \begin{bmatrix} 2 & -1 & 2 \\ 2 & 2 & -1 \\ -1 & 2 & 2 \end{bmatrix} \begin{bmatrix} u' \\ v' \\ w' \end{bmatrix}_2$$

By inspection the three smallest non-coplanar g_c vectors, indexed with respect to grain 1, are $(111)_1$, $(20\bar{2})_1$ and $(02\bar{2})_1$, giving the g_c matrix and its inverse as, respectively,

$$\begin{bmatrix} 1 & 1 & 1 \\ 2 & 0 & -2 \\ 0 & 2 & -2 \end{bmatrix}, \qquad \frac{1}{6} \begin{bmatrix} 2 & 2 & -1 \\ 2 & -1 & 2 \\ 2 & -1 & -1 \end{bmatrix},$$

so that the basis DSC vectors for this $\Sigma 3$ CSL are $\frac{1}{3}[111]_1$, $\frac{1}{6}[2\bar{1}\bar{1}]_1$ and $\frac{1}{6}[\bar{1}2\bar{1}]_1$. For boundaries with other Σ values the magnitudes of the g_c vectors increase and the magnitudes of the DSC vectors decrease with increasing Σ value.

The methods available for the determination of the Burgers vectors of GBDs from their electron diffraction contrast in bright field images are more restricted than those for dislocations in single crystals. For example, the criteria $\boldsymbol{g} \cdot \boldsymbol{b} = 0$ can only conceivably be applied under two rather restrictive conditions: (i) when a bicrystal is orientated with respect to the electron beam so that only one grain is diffracting in 'two-beam' conditions, with the second grain nominally 'non-diffracting', and (ii) when the same diffracting vector g_c is operating under two-beam conditions in both grains (Barry and Mahajan 1971). Condition (i) cannot be used with any reliability because $\boldsymbol{g} \cdot \boldsymbol{b}$ frequently has small fractional values and the resultant weak diffraction contrast cannot be reliably distinguished from cases where $\boldsymbol{g} \cdot \boldsymbol{b} = 0$. In addition, the diffraction contrast always arises from a GBD lying in an entrance or exit surface for the electron beam in the diffracting crystal, and under these conditions it is known that $\boldsymbol{g} \cdot \boldsymbol{b} = 0$ criteria are very unreliable (Clarebrough 1974). In the case of condition (ii), $g_c \cdot \boldsymbol{b}$ has integral values (since the g_c lattice is reciprocal to the DSC lattice) so that, similar to the case of dislocations in single crystals, the $g_c \cdot \boldsymbol{b} = 0$ condition can in principle be distinguished. However, there is a very restricted set of g_c vectors available for a given boundary and, for boundaries with high values of Σ, some of the required g_c vectors are of such high order that it is virtually impossible to set good two-beam diffraction conditions. In addition, there are rigid body displacements between neighbouring grains for many near CSL boundaries (Pond and Vitek 1977;

* The rotation axis corresponding to the matrix $(\boldsymbol{P}, \omega)$ always gives one of the same g_c vectors and the others can often be obtained by simple inspection of the $(\boldsymbol{P}, \omega)$ matrix. However, when simple inspection fails, the general form of the indices $\langle h, k, l \rangle$ of the other same g_c vectors is given by the rotation axes of the matrices obtained by operating on the $(\boldsymbol{P}, \omega)$ matrix with the symmetry matrices for cubic crystals.

Forwood and Clarebrough 1983, 1984, 1985), and these displacements give rise to fringe contrast in the boundary which influences the visibility of the GBDs. For example, situations commonly arise in which GBDs show strong diffraction contrast when $\boldsymbol{g}_c \cdot \boldsymbol{b} = 0$. For these reasons $\boldsymbol{g} \cdot \boldsymbol{b} = 0$ criteria cannot be used with confidence even for condition (ii).

The difficulties associated with the determination of the Burgers vectors of GBDs are overcome by using the method of image matching for GBDs (Humble and Forwood 1975; Forwood and Humble 1975). This is based on the technique of image matching for dislocations in single crystals (Head *et al.* 1973), in which experimental images of a dislocation are compared with theoretical images computed for different Burgers vectors.* For GBDs the experimental images used are ones in which both grains are diffracting simultaneously under good two-beam diffraction conditions. In general, different diffracting vectors are used in each grain, but the method can be used equally well with the same $\boldsymbol{g}_c$ diffracting vector in both grains. Theoretical images are computed using the 'welded' boundary approximation for calculating the displacement field of a GBD in anisotropic elasticity (Tucker 1969) so that they apply to an isolated GBD in a boundary. However, the technique can be applied to a GBD in a network provided that the spacing of the dislocations in the network is sufficiently large for the local elastic displacement field of the GBD, causing the diffraction contrast, to be represented by that of an isolated GBD. The method has the advantage that it enables the magnitude and sense of a GBD to be determined.

Table 1. Diffraction parameters

Diffracting vector $\boldsymbol{g}$	Extinction distance ξ_g (Å)	Anomalous absorption
111	416	0·07
200	469	0·08
220	675	0·10
311	817	0·11

3. Experimental Details

The material used was a Cu +6 at.% Si alloy in the form of an annealed strip 75 μm thick. Small tensile specimens were cut from this strip, strained 5% and annealed for 1 h at 600°C under vacuum to produce an average grain size of approximately 20 μm. After thinning, specimens were examined by transmission electron microscopy at 200 kV, by using a goniometer stage giving ±30° of tilt about two orthogonal axes.

Grain boundaries of the type Σ3, Σ9, Σ27 and Σ81 were commonly observed, and the near Σ9, Σ27a, Σ27b and Σ81a boundaries, selected for detailed analysis, were inclined at shallow angles in the foils with misorientations very close ($\lesssim$ 0·1°) to exact CSL orientations, so that the dislocations in the secondary GBD networks were widely spaced.

For computing theoretical images the elastic constants used were C_{11} = 16·58,

* The theoretical images presented in this paper have been computed using a 'Corona' personal computer and the images have been produced on an 'Epson FX 80' printer using 25 levels of grey.

$C_{12} = 12{\cdot}64$ and $C_{44} = 7{\cdot}41 \times 10^{10}\ \mathrm{N\,m^{-2}}$ (Neighbours and Smith 1954). The values of extinction distance and anomalous absorption for different diffracting vectors are given in Table 1. The determination of crystallographic data, such as boundary planes and directions of dislocations, was made using standard stereographic analysis from images and diffraction patterns taken in at least four different beam directions spanning the full range of tilt.

For all the boundaries considered, the boundary plane normals are taken as pointing from the lower grain, with respect to the electron source, into the upper grain, while the sense of the line directions of the GBDs is taken as pointing from the bottom surface of the foil, with respect to the electron source, to the top surface of the foil.

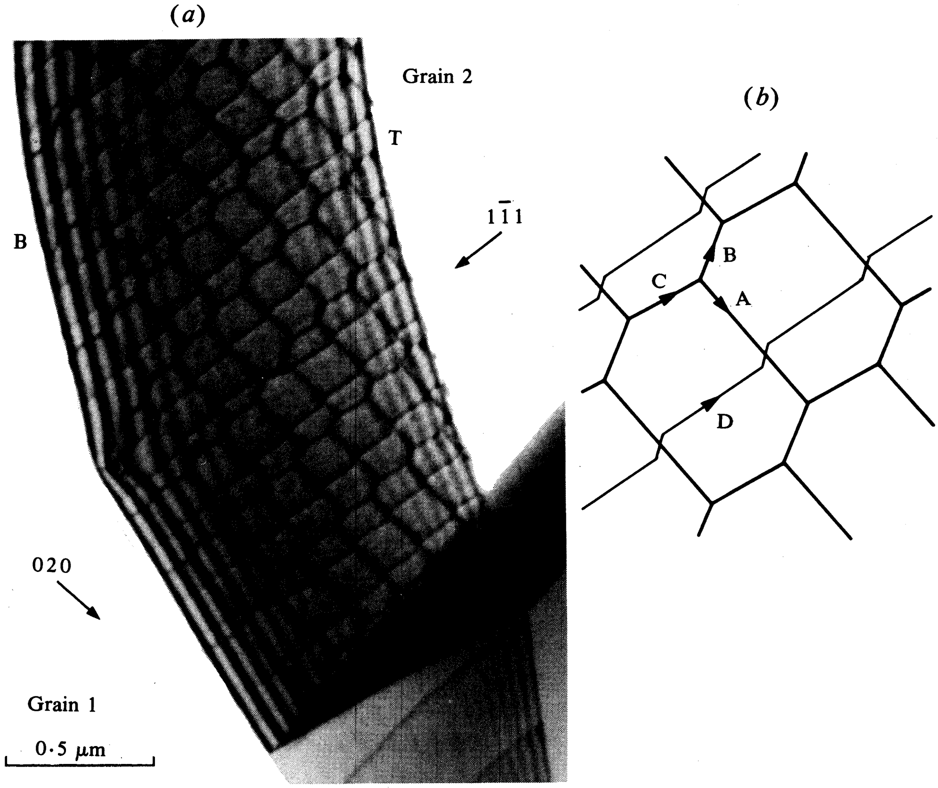

Fig. 1. Simultaneous two-beam electron micrograph (*a*) showing a secondary GBD network in a near Σ9 boundary. The intersections of the boundary with the bottom and top of the foil with respect to the electron source are the traces marked B and T respectively, so that grain 1 is the upper grain. The diffracting vectors are indicated and the beam directions are close to $[\bar{1}05]_1$ and $[\bar{3}14]_2$. A schematic representation of the secondary GBD network is shown in (*b*).

4. Results

In this section the Burgers vectors of the dislocations forming the secondary GBD networks in near Σ9, Σ27a, Σ27b and Σ81a boundaries will be identified using the image matching technique. With this technique, it is necessary to use a sufficient number of experimental images so that the diffracting vectors involved sample the

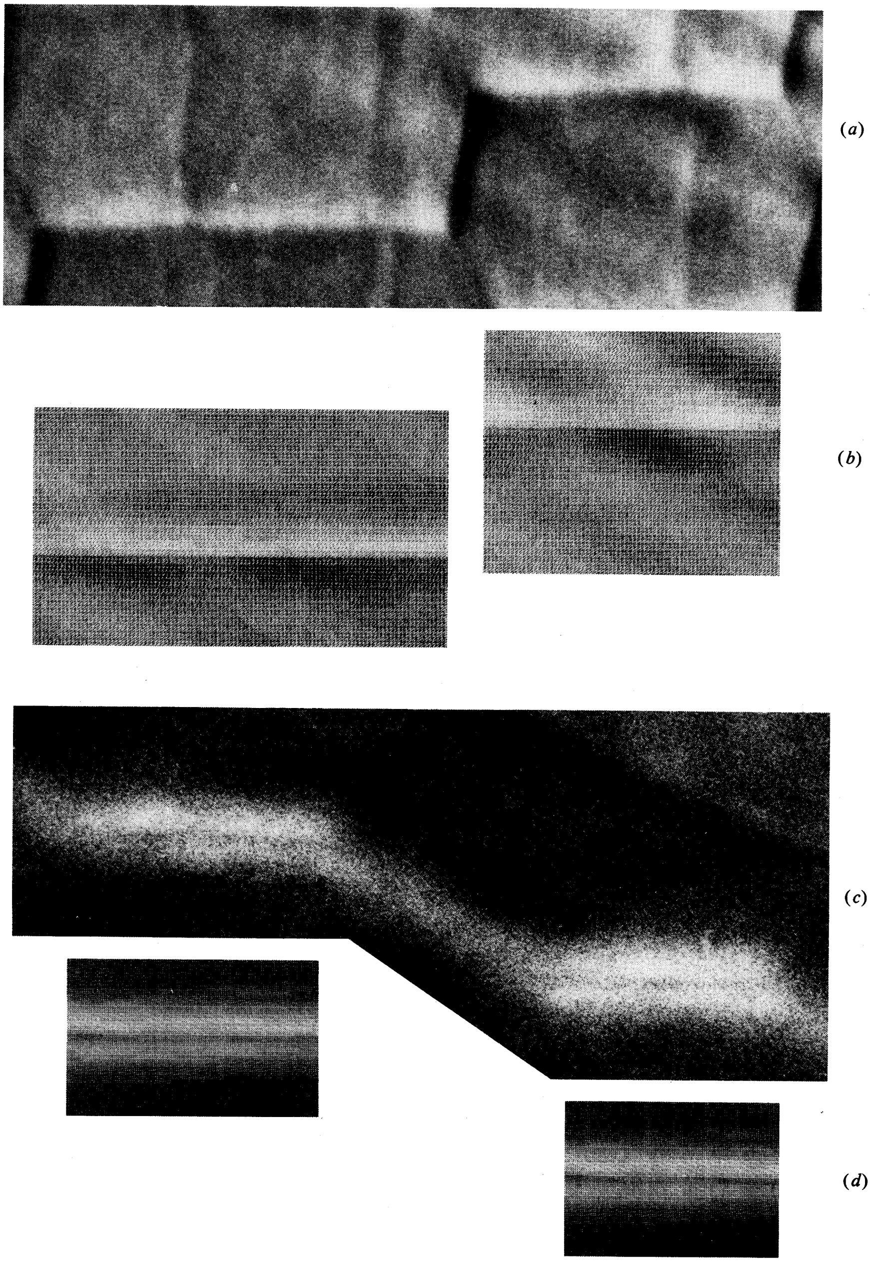

Fig. 2. Experimental and theoretical electron micrographs of secondary GBDs in a near $\Sigma 9$ boundary with boundary normal $[439]_1$ in a foil $13 \cdot 5\ \xi_{111}$ thick with foil normal $[\bar{5}\,19\,27]_1$. The experimental electron micrographs (*a*), (*c*), (*e*) and (*h*) have diffraction vectors $\boldsymbol{g}$, beam directions $\boldsymbol{B}$ (values listed here and in Figs 4, 5, 7, 9–11 are close to actual values), deviation parameter w, and GBD line directions $\boldsymbol{l}$ as listed opposite. The matching theoretical images (*b*) were computed for the parameters of (*a*) with $\boldsymbol{b}_{\mathrm{A}} = \frac{1}{9}[1\bar{2}2]_1$. Similarly (*d*) was computed for the parameters of (*c*) with $\boldsymbol{b}_{\mathrm{B}} = \frac{1}{18}[1\bar{2}\bar{7}]_1$; (*f*) and (*g*) were computed for the parameters in (*e*) for C and B respectively with $\boldsymbol{b}_{\mathrm{C}} = \frac{1}{6}[1\bar{2}\bar{1}]_1$ and $\boldsymbol{b}_{\mathrm{B}} = \frac{1}{18}[1\bar{2}\bar{7}]_1$; and (*i*) was computed for parameters of (*h*) with $\boldsymbol{b}_{\mathrm{D}} = \frac{1}{18}[41\bar{1}]_1$.

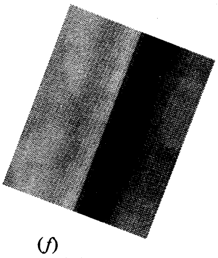

(*f*)

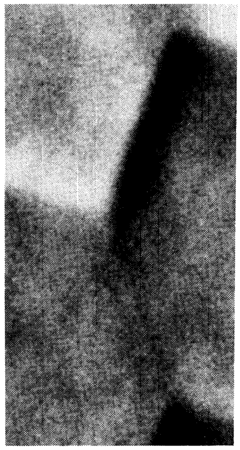

(*e*)

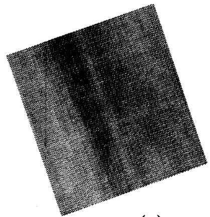

(*g*)

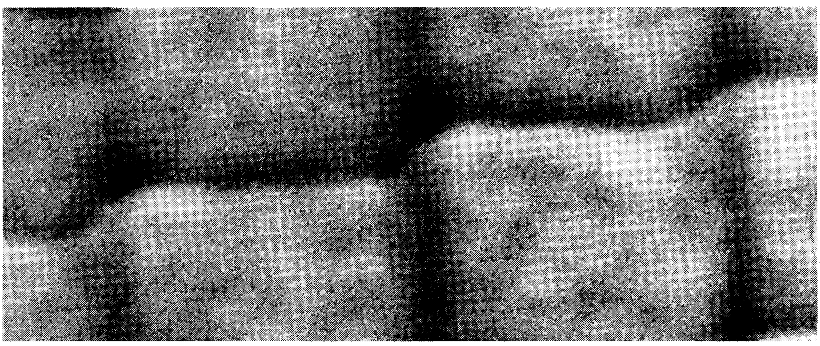

(*h*)

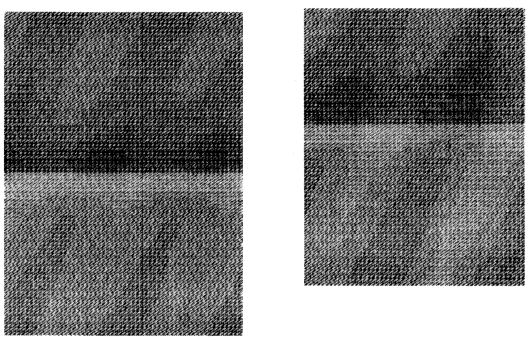

(*i*)

Fig.	GBD	$\boldsymbol{g}$	$\boldsymbol{B}$	w	$\boldsymbol{l}$
(*a*)	A	020_1	$[\bar{1}05]_1$	$0\cdot35_1$	$[03\bar{1}]_1$
		$\bar{1}1\bar{1}_2$	$[\bar{3}14]_2$	$0\cdot29_2$	
(*c*)	B	020_1	$[105]_1$	$0\cdot20_1$	$[\overline{24}\,\overline{13}\,15]_1$
		020_2	$[\bar{1}03]_2$	$0\cdot20_2$	
(*e*)	C	As for Fig. 2*a*			$[\overline{18}\,3\,7]_1$
	B				$[\overline{24}\,\overline{13}\,15]_1$
(*h*)	D	020_1	$[\bar{1}05]_1$	$0\cdot40_1$	$[\overline{60}\,\bar{1}\,27]_1$
		$1\bar{1}1_2$	$[\bar{3}14]_2$	$0\cdot40_2$	

full three-dimensional displacement field of the GBD under consideration. For two-beam diffracting conditions each diffracting vector g samples only the component of the displacement field parallel to g, so that images involving at least three non-coplanar diffracting vectors are needed. Each of the experimental images selected is compared with theoretical images computed for the possible Burgers vectors that could apply to the GBD under consideration. In this way, the Burgers vectors which give mismatching theoretical images are eliminated, so that the matching set of theoretical images defines the Burgers vector. For secondary GBDs the possible Burgers vectors are the basis DSC vectors for a particular Σ value and all linear combinations of these vectors. However, in this work, for all the boundaries considered, the possible Burgers vectors tested with theoretical images were restricted to those with magnitudes up to and including the magnitude of a $\frac{1}{6}\langle 112\rangle$ vector.

It is not possible here to show all the experimental images with the matching and mismatching theoretical images that were used and only selected examples will be presented. For example, in the case of the near $\Sigma 9$ and near $\Sigma 27$b boundaries only one matching pair of experimental and theoretical images, for each of the components of the GBD network, are presented; in the case of the near $\Sigma 27$a boundary an example of the use of three non-coplanar diffracting vectors is demonstrated, and in the case of the near $\Sigma 81$a boundary some mismatching theoretical images are included.

(a) Near Σ 9 Boundary

Fig. 1*a* shows a low magnification image of a portion of a near $\Sigma 9$ boundary which terminates at the bottom right of the micrograph in a triple junction involving a coherent $\Sigma 3$ and a near $\Sigma 27$ boundary. The small angular departure from the exact $\Sigma 9$ orientation is taken up by the coarse secondary GBD network, which is clearly resolved in Fig. 1*a* and illustrated schematically in Fig. 1*b*. The network consists of three independent arrays of GBDs, A, B and D, in which the segments A and B have interacted to form the GBD product C, giving a hexagonal network in the boundary containing elements with the three Burgers vectors $\boldsymbol{b}_A$, $\boldsymbol{b}_B$ and $\boldsymbol{b}_C$, where $\boldsymbol{b}_C = \boldsymbol{b}_A + \boldsymbol{b}_B$. The dislocation D with Burgers vector $\boldsymbol{b}_D$ crosses the segments A of the hexagonal array and, although it changes direction where it crosses segments A, it does not interact to form reaction products.

The exact CSL orientation corresponding to this near $\Sigma 9$ boundary involves a clockwise rotation of grain 2 with respect to grain 1 by 38·94° around an axis parallel to [011] in both grains, and is defined by the matrix

$$\frac{1}{9}\begin{bmatrix} 7 & -4 & 4 \\ 4 & 8 & 1 \\ -4 & 1 & 8 \end{bmatrix},$$

which transforms a direction indexed with respect to grain 2 into that indexed with respect to grain 1. The same g_c matrix, indexed with respect to grain 1, is

$$\begin{bmatrix} 0 & 2 & 2 \\ 4 & 2 & 0 \\ 1 & -3 & 1 \end{bmatrix}_1,$$

which gives the basis DSC vectors as $\boldsymbol{a} = \frac{1}{18}[41\bar{1}]_1$, $\boldsymbol{b} = \frac{1}{9}[1\bar{2}2]_1$ and $\boldsymbol{c} = \frac{1}{18}[1\bar{2}\bar{7}]_1$.

Fig. 2 shows matching theoretical and experimental images for the segments A, B, D and the reaction product C of the secondary GBD network, where the theoretical images were computed for $\boldsymbol{b}_{\mathrm{A}} = \frac{1}{9}[1\bar{2}2]_1$, $\boldsymbol{b}_{\mathrm{B}} = \frac{1}{18}[12\bar{7}]_1$, $\boldsymbol{b}_{\mathrm{C}} = \frac{1}{6}[1\bar{2}\bar{1}]_1$ and $\boldsymbol{b}_{\mathrm{D}} = \frac{1}{18}[41\bar{1}]_1$. For segment A (Figs 2*a* and 2*b*), B (Figs 2*c* and 2*d*) and D (Figs 2*h* and 2*i*), the theoretical images were computed for two segments at different depths in the foil and in these figures the images of the GBDs are arranged to be horizontal. The experimental image Fig. 2*e* shows the GBDs A (centre left), B (lower) and C (upper) meeting at a node. The matching theoretical image for the reaction product C is shown in Fig. 2*f* and the matching theoretical image for the segment B, under these diffracting conditions, is shown in Fig. 2*g*.

The character of the experimental images in Figs 2*a* and 2*h* is typical of that found for secondary GBDs and involves a change from black to white contrast at the line of the GBD. It was found that a great many possibilities for the Burgers vectors of GBDs could be eliminated simply on the basis of whether, in computed images, black and white contrast appeared on the appropriate sides of the GBD. In some cases special features of contrast involving fine detail helped in the identification, and such an example is shown in Figs 2*c* and 2*d* where the contrast of GBD B consists of a narrow black line (approximately 3 nm wide) bordered by two diffuse white bands.

Image matching of the type illustrated in Fig. 2 identified the Burgers vectors of the GBDs as $\boldsymbol{b}_{\mathrm{A}} = \boldsymbol{b} = \frac{1}{9}[1\bar{2}2]_1$, $\boldsymbol{b}_{\mathrm{B}} = \boldsymbol{c} = \frac{1}{18}[12\bar{7}]_1$, $\boldsymbol{b}_{\mathrm{C}} = \boldsymbol{b}+\boldsymbol{c} = \frac{1}{6}[1\bar{2}\bar{1}]_1$ and $\boldsymbol{b}_{\mathrm{D}} = \boldsymbol{a} = \frac{1}{18}[41\bar{1}]_1$. The identified Burgers vectors show that the three independent arrays of GBDs A, B and D have basis Σ9 DSC Burgers vectors and that the GBD C is the reaction product formed by the reaction

$$\boldsymbol{b}_{\mathrm{C}} = \boldsymbol{b}_{\mathrm{A}} + \boldsymbol{b}_{\mathrm{B}}\,,$$

i.e. $\frac{1}{6}[1\bar{2}\bar{1}]_1 = \frac{1}{9}[1\bar{2}2]_1 + \frac{1}{18}[12\bar{7}]_1$, which is an energy lowering reaction on the simple $\boldsymbol{b}^2$ criterion (Frank 1949).

(b) Near Σ27a Boundary

Fig. 3*a* shows a low magnification image of part of a near Σ27a boundary. The course secondary GBD network in the boundary, which accommodates the small departure of the misorientation between grains 1 and 2 from the exact Σ27a CSL orientation, contains three independent arrays of GBDs, A, B and D, as illustrated schematically in Fig. 3*b*. The GBD segments A, B and C, with Burgers vectors $\boldsymbol{b}_{\mathrm{A}}$, $\boldsymbol{b}_{\mathrm{B}}$ and $\boldsymbol{b}_{\mathrm{C}}$, form a hexagonal network in which C is the reaction product formed by the interaction of A and B. The GBDs D with Burgers vector $\boldsymbol{b}_{\mathrm{D}}$ cross the elements of the hexagonal network without reacting.

The exact CSL orientation corresponding to this near Σ27a boundary involves a clockwise rotation of grain 2 with respect to grain 1 by 31·58° around an axis parallel to [011] in both grains, and is defined by the matrix

$$\frac{1}{27}\begin{bmatrix} 23 & -10 & 10 \\ 10 & 25 & 2 \\ -10 & 2 & 25 \end{bmatrix}.$$

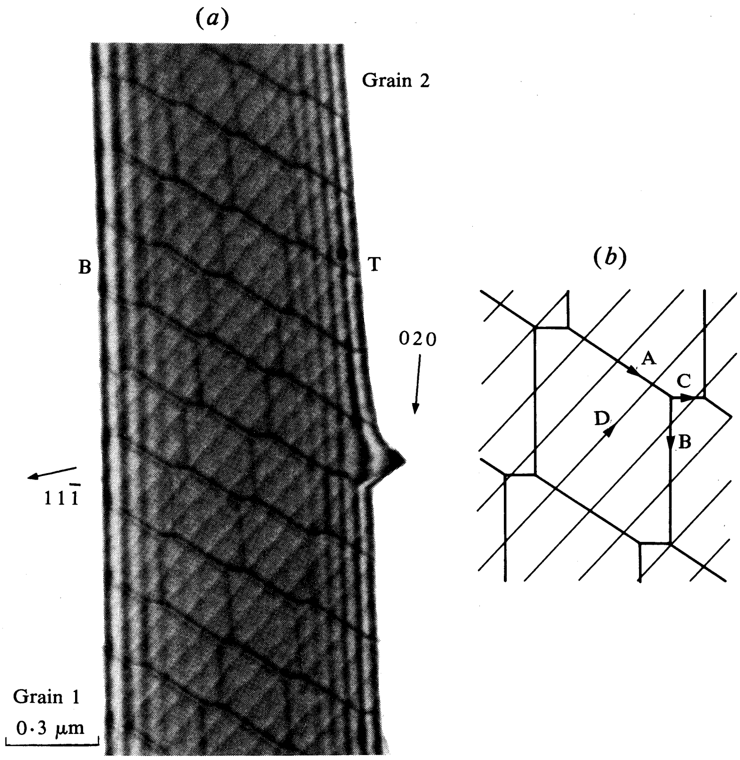

Fig. 3. Simultaneous two-beam electron micrograph (*a*) showing a secondary GBD network in a near Σ27a boundary. The intersections of the boundary with the bottom and top of the foil with respect to the electron source are the traces marked B and T respectively, so that grain 1 is the upper grain. The diffracting vectors are indicated and the beam directions are close to $[314]_1$ and $[103]_2$. A schematic representation of the secondary GBD network is shown in (*b*).

The same g_c matrix indexed with respect to grain 1 is therefore

$$\begin{bmatrix} 0 & 2 & 2 \\ -5 & -1 & 1 \\ 2 & -6 & 4 \end{bmatrix}_1 ,$$

which gives the basis DSC vectors as $\boldsymbol{a} = \frac{1}{54}[1\,11\,16]_1$, $\boldsymbol{b} = \frac{1}{27}[\bar{5}\bar{1}1]_1$ and $\boldsymbol{c} = \frac{1}{54}[2\bar{5}5]_1$.

Matching experimental and theoretical images for the segments A, B and D of the secondary GBD network of this near Σ27a boundary are shown in Figs 4 and 5, where the theoretical images were computed for $\boldsymbol{b}_A = \frac{1}{6}[\bar{1}12]_1$, $\boldsymbol{b}_B = \frac{1}{27}[\bar{5}\bar{1}1]_1$ and $\boldsymbol{b}_D = \frac{1}{54}[2\bar{5}5]_1$. The images for two segments of A at different depths in the foil, and for three different sets of diffracting conditions, are given in Figs 4*a–c*; the images for segment B, for two different diffracting conditions, are given in Figs 5*a* and 5*b*, and the images for segment D are given in Fig. 5*c*. In all cases the GBD under consideration is arranged to be horizontal in the figures. The three experimental images, and matching theoretical images computed for $\boldsymbol{b}_A = \frac{1}{6}[\bar{1}12]_1$ in Fig. 4, are

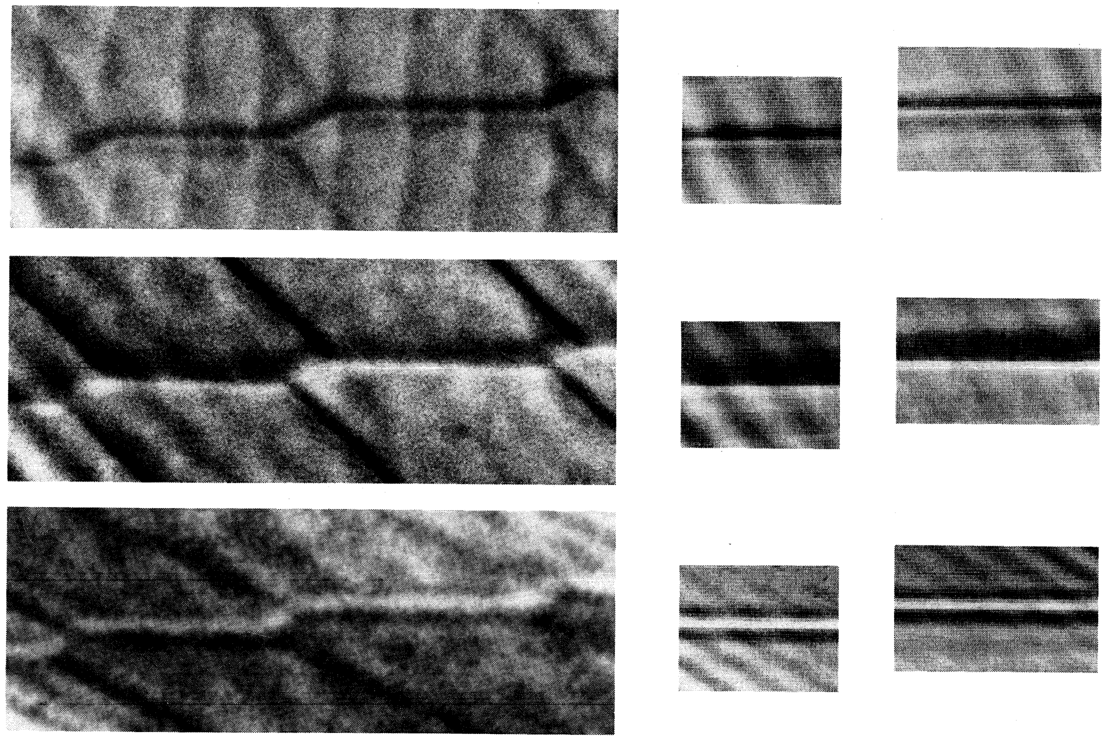

Fig. 4. Experimental and theoretical electron micrographs of the secondary GBD A of Fig. 3. The GBD line direction $\boldsymbol{l}$ is $[\bar{1}\bar{1}\,4\,16]_1$, the boundary normal is $[432]_1$, the foil thickness is $15\cdot 8\xi_{111}$ and the foil normal is $[6\,9\,22]_1$. The diffraction parameters for the experimental images and the theoretical images computed for $\boldsymbol{b}_A = \frac{1}{6}[\bar{1}12]_1$ are:

Fig.	$\boldsymbol{g}$	$\boldsymbol{B}$	w	Fig.	$\boldsymbol{g}$	$\boldsymbol{B}$	w	Fig.	$\boldsymbol{g}$	$\boldsymbol{B}$	w
(*a*)	$11\bar{1}_1$	$[314]_1$	$0\cdot 30_1$	(*b*)	020_1	$[409]_1$	$0\cdot 40_1$	(*c*)	200_1	$[0\,\bar{1}\,11]_1$	$0\cdot 43_1$
	020_2	$[103]_2$	$0\cdot 22_2$		$\bar{2}00_2$	$[0\,\bar{1}\,11]_2$	$0\cdot 02_2$		$0\bar{2}0_2$	$[\bar{4}09]_2$	$0\cdot 43_2$

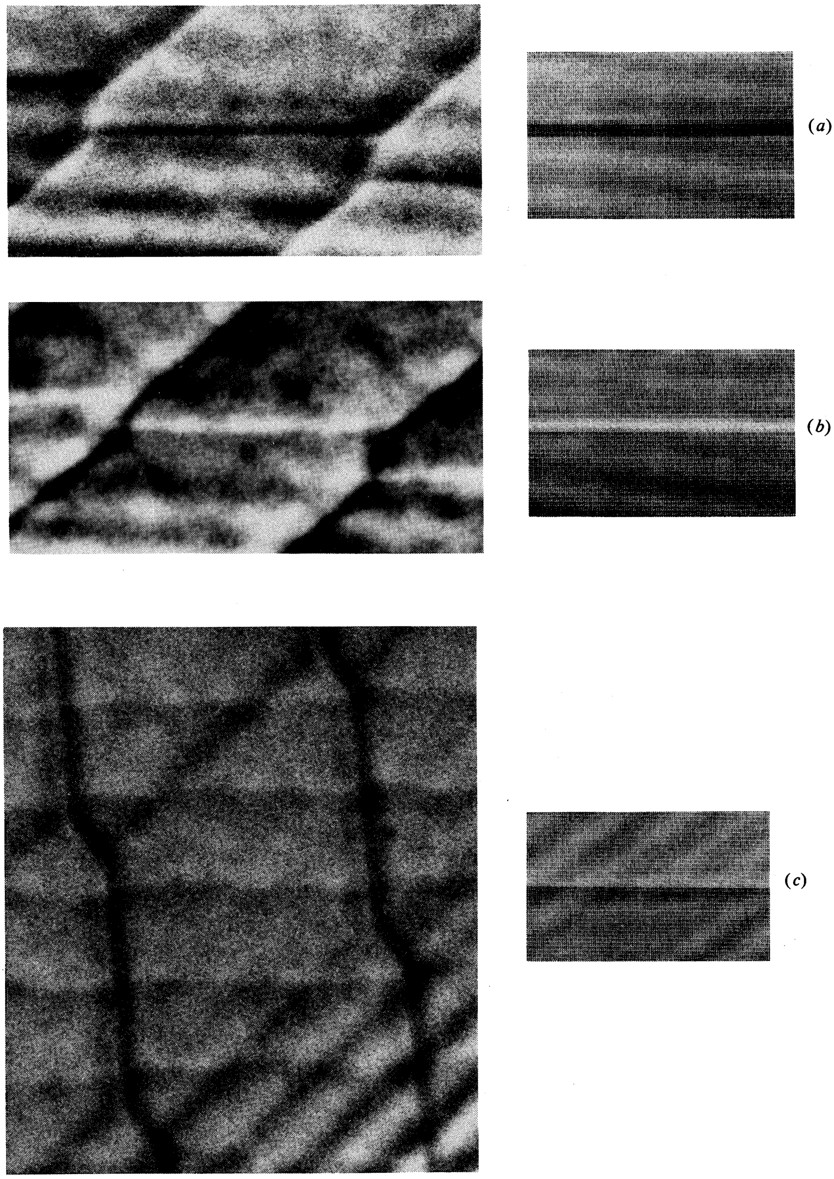

Fig. 5. Experimental and theoretical electron micrographs of the secondary GBDs B (*a*) and (*b*), and D (*c*) of Fig. 3. The boundary normal, foil thickness and foil normal are given in Fig. 4 and the GBD line directions $\boldsymbol{l}$ are $[27\,\overline{56}\,78]_1$ for B and $[9\,\overline{34}\,33]_1$ for D. The diffraction parameters for the experimental images and the theoretical images, computed for $\boldsymbol{b}_{\mathrm{B}} = \frac{1}{27}[\bar{5}\bar{1}1]_1$ and $\boldsymbol{b}_{\mathrm{D}} = \frac{1}{54}[2\bar{5}5]_1$, are:

Fig.	GBD	$\boldsymbol{g}$	$\boldsymbol{B}$	w
(*a*)	B	020_1	$[409]_1$	$0\cdot40_1$
		$\bar{2}00_2$	$[0\,\bar{1}\,11]_2$	$0\cdot02_2$
(*b*)	B	$0\bar{2}0_1$	$[409]_1$	$0\cdot40_1$
		200_2	$[0\,\bar{1}\,11]_2$	$0\cdot02_2$
(*c*)	D	$11\bar{1}_1$	$[314]_1$	$0\cdot30_1$
		020_2	$[103]_2$	$0\cdot22_2$

for three sets of diffracting conditions involving non-coplanar diffracting vectors which sample the full three-dimensional displacement field of the GBD. These experimental and matching theoretical images, which cover a wide range of image character [black–white contrast in (*b*) and double images with different character in (*a*) and (*c*)], illustrate the degree of agreement obtained in the image matching technique, which leads to the positive identification of the Burgers vectors of GBDs. The experimental images and matching theoretical images computed for $\boldsymbol{b}_{\mathrm{B}} = \frac{1}{27}[5\bar{1}1]_1$ in Figs 5*a* and 5*b* illustrate the change in contrast of a GBD (i.e. reversal from black to white) that results from reversing the sign of the diffracting vectors in both grains.

Image matching identified the Burgers vectors of the GBD segments A, B and D as $\boldsymbol{b}_{\mathrm{A}} = \boldsymbol{a}+\boldsymbol{b} = \frac{1}{6}[\bar{1}12]_1$, $\boldsymbol{b}_{\mathrm{B}} = \boldsymbol{b} = \frac{1}{27}[5\bar{1}1]_1$ and $\boldsymbol{b}_{\mathrm{D}} = \boldsymbol{c} = \frac{1}{54}[2\bar{5}5]_1$. The Burgers vector of the short segment C was also identified by image matching as $\boldsymbol{b}_{\mathrm{C}} = \boldsymbol{a} = \frac{1}{54}[1\ 11\ 16]_1$ but no matching experimental and theoretical images are shown here. This Burgers vector is the reaction product formed by the energy lowering reaction

$$\boldsymbol{b}_{\mathrm{C}} = \boldsymbol{b}_{\mathrm{A}} - \boldsymbol{b}_{\mathrm{B}}\,.$$

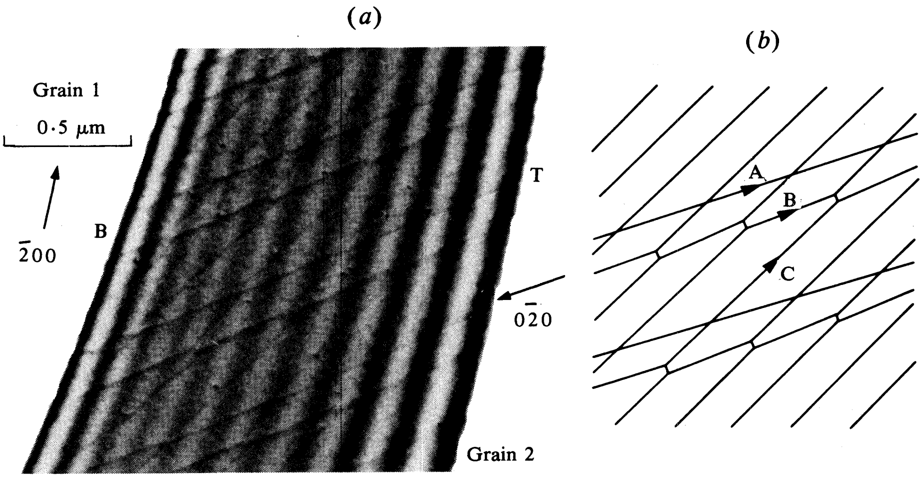

Fig. 6. Simultaneous two-beam electron micrograph (*a*) showing a secondary GBD network in a near Σ27b boundary. The intersections of the boundary with the bottom and top of the foil with respect to the electron source are the traces marked B and T respectively, so that grain 1 is the upper grain. The diffracting vectors are indicated and the beam directions are close to $[0\bar{1}12]_1$ and $[301]_2$. A schematic representation of the secondary GBD network is shown in (*b*).

(c) Near Σ27b Boundary

Fig. 6*a* shows a low magnification image of a near Σ27b boundary where the secondary GBD network contains three independent arrays of GBDs A, B and C as illustrated schematically in Fig. 6*b*. In the network, segments B and C interact where they cross to form very short lengths of reaction product, whereas segment A does not react with segment C.

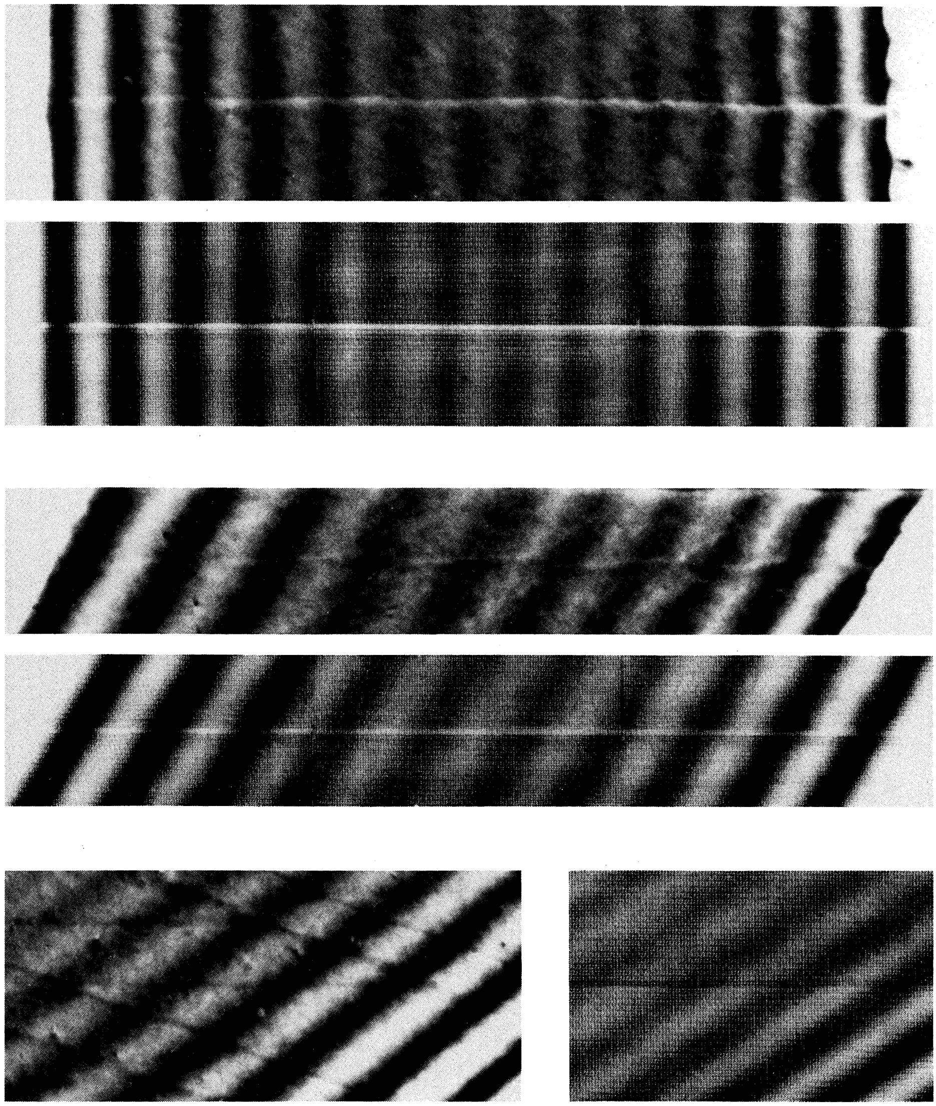

(a)

(b)

(c)

Fig. 7. Matching experimental and theoretical images for the secondary GBDs (*a*) A, (*b*) B and (*c*) C in the network of Fig. 6. The boundary normal is $[\bar{2}\bar{6}7]_1$, and the foil is $11\cdot0\xi_{111}$ thick with foil normal $[\bar{4}\bar{7}\,14]_1$. The diffraction parameters and line directions of the GBDs $\boldsymbol{l}$ are:

Fig.	GBD	$\boldsymbol{g}$	$\boldsymbol{B}$	w	$\boldsymbol{l}$
(*a*)	A	$1\bar{1}1_1$	$[\bar{9}\bar{1}8]_1$	$0\cdot20_1$	$[\bar{2}32]_1$
		$\bar{1}\bar{1}1_2$	$[112]_2$	$0\cdot12_2$	
(*b*)	B	200_1	$[0\,\bar{1}\,12]_1$	$0\cdot30_1$	$[\bar{2}32]_1$
		$0\bar{2}0_2$	$[301]_2$	$0\cdot10_2$	
(*c*)	C	$\bar{2}00_1$	$[0\,\bar{1}\,12]_1$	$0\cdot02_1$	$[\bar{8}\bar{3}\,51\,20]_1$
		$0\bar{2}0_2$	$[301]_2$	$0\cdot44_2$	

The matching theoretical images were computed for $\boldsymbol{b}_{\mathrm{A}} = \frac{1}{54}[1\,\overline{19}\,\bar{4}]_1$, $\boldsymbol{b}_{\mathrm{B}} = \frac{1}{18}[\bar{1}14]_1$ and $\boldsymbol{b}_{\mathrm{C}} = \frac{1}{54}[\bar{7}\bar{2}1]_1$.

The exact CSL orientation corresponding to this near Σ27b boundary involves a clockwise rotation of grain 2 with respect to grain 1 by 79·33° around an axis parallel to $[1\bar{3}1]$ in both grains, and is defined by the matrix

$$\frac{1}{27}\begin{bmatrix} 7 & -14 & -22 \\ 2 & 23 & -14 \\ 26 & 2 & 7 \end{bmatrix}.$$

The same g_c matrix indexed with respect to grain 1 is therefore

$$\begin{bmatrix} 1 & -3 & 1 \\ 0 & 2 & 4 \\ 7 & 3 & 1 \end{bmatrix}_1,$$

which gives the basis DSC vectors as $\boldsymbol{a} = \frac{1}{54}[5\,\overline{14}\,7]_1$, $\boldsymbol{b} = \frac{1}{18}[\bar{1}14]_1$ and $\boldsymbol{c} = \frac{1}{54}[\bar{7}\bar{2}1]_1$.

Figs 7*a–c* show matching experimental and theoretical images for the segments A, B and C respectively of this near Σ27b boundary, where the theoretical images were computed for $\boldsymbol{b}_A = \frac{1}{54}[1\,\overline{19}\,\bar{4}]_1$, $\boldsymbol{b}_B = \frac{1}{18}[\bar{1}14]_1$ and $\boldsymbol{b}_C = \frac{1}{54}[\bar{7}\bar{2}1]_1$. In all cases the relevant GBD segment is arranged to be horizontal in the figure, and segments A and B were computed throughout the full thickness of the foil, whilst segment C was

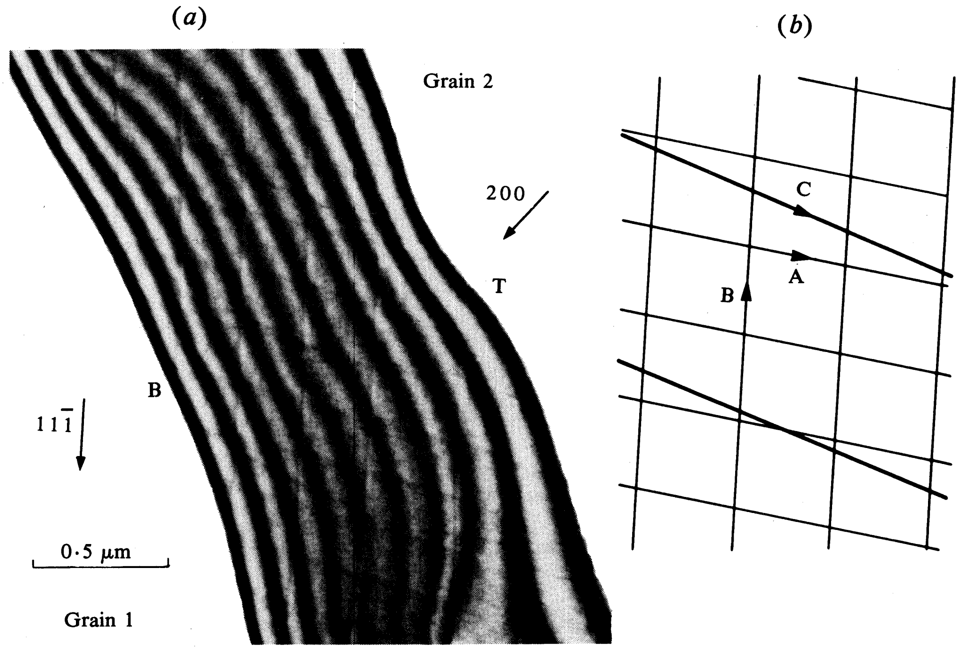

Fig. 8. Simultaneous two-beam electron micrograph (*a*) showing a secondary GBD network in a near Σ81a boundary. The intersections of the boundary with the bottom and top of the foil with respect to the electron source are the traces marked B and T respectively, so that grain 1 is the upper grain. The diffracting vectors are indicated and the beam directions are close to $[\bar{3}52]_1$ and $[\bar{1}45]_2$. A schematic representation of the secondary GBD network is shown in (*b*).

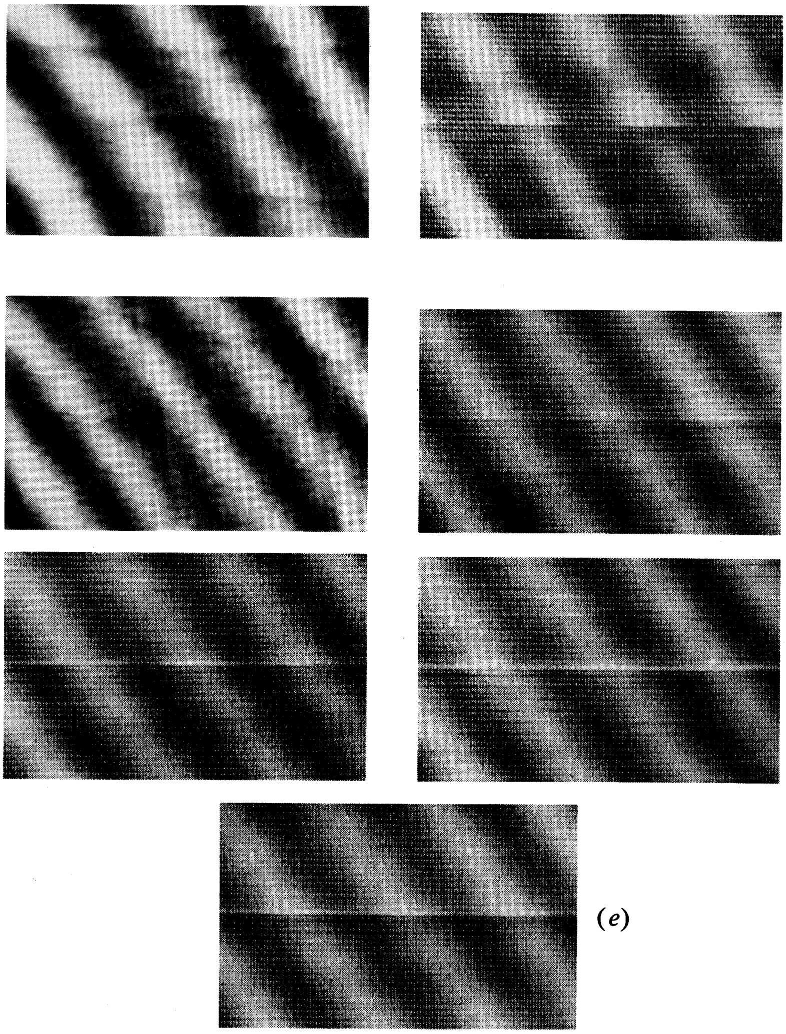

Fig. 9. Matching experimental and theoretical images (*a*) and (*b*), for GBD A of Fig. 8 for $\boldsymbol{b}_A = \frac{1}{162}[11\,13\,14]_1$. The GBD line direction $\boldsymbol{l}$ is $[\bar{6}35]_1$, the boundary normal is $[\bar{1}\,43\,27]_1$, the foil thickness is $9\cdot3\xi_{111}$ and the foil normal is $[\bar{7}\,\overline{21}\,12]_1$. The diffraction parameters are:

Fig.	$\boldsymbol{g}$	$\boldsymbol{B}$	w
(*a*)	$02\bar{2}_1$	$[\bar{1}\,11\,11]_1$	$0\cdot14_1$
	$\bar{2}20_2$	$[115]_2$	$0\cdot0_2$
(*b*)	$1\bar{1}1_1$	$[\bar{3}52]_1$	$0\cdot36_1$
	$\bar{1}1\bar{1}_2$	$[\bar{1}34]_2$	$0\cdot21_2$

The additional theoretical images (*c*)–(*e*) were computed for the diffraction parameters of (*b*) with $\boldsymbol{b}_A = \frac{1}{162}[17\,2\,29]_1$, (*c*); $\boldsymbol{b}_A = \frac{1}{162}[23\,17\,44]_1$, (*d*); and $\boldsymbol{b}_A = \frac{1}{162}[28\,\overline{11}\,43]_1$, (*e*).

computed between two nodal points in the GBD network. In the theoretical image in Fig. 7*b*, no account was taken of the fact that in the experimental image of B there are interactions at various positions along its length with segment C. However, this did not interfere with the identification of the Burgers vector of this GBD by image matching.

The full image matching procedure identified the Burgers vectors of the segments A, B and C as $\boldsymbol{b}_A = \boldsymbol{a}-\boldsymbol{b}+\boldsymbol{c} = \frac{1}{54}[1\,\overline{19}\,\overline{4}]_1$, $\boldsymbol{b}_B = \boldsymbol{b} = \frac{1}{18}[\overline{1}14]_1$ and $\boldsymbol{b}_C = \boldsymbol{c} = \frac{1}{54}[\overline{7}\overline{2}1]_1$. The lengths of GBD formed by the interaction of B and C were too short to be reliably identified by image matching, but their Burgers vector would correspond to $\boldsymbol{b}_B - \boldsymbol{b}_C = \frac{1}{54}[4\,5\,11]_1$.

(d) Near $\Sigma 81a$ Boundary

Fig. 8*a* shows a low magnification image of a near Σ81a boundary where the secondary GBD network contains three independent arrays of GBDs A, B and C, as illustrated schematically in Fig. 8*b*.

The exact CSL orientation corresponding to this near Σ81a boundary involves a clockwise rotation of grain 2 with respect to grain 1 by 38·38° around an axis parallel to $[\overline{5}\overline{1}3]$ in both grains and is defined by the matrix,

$$\frac{1}{81}\begin{bmatrix} 76 & -23 & -16 \\ 28 & 64 & 41 \\ 1 & -44 & 68 \end{bmatrix}.$$

The same g_c matrix indexed with respect to grain 1 is therefore

$$\begin{bmatrix} -5 & -1 & 3 \\ 2 & 6 & 4 \\ -5 & 5 & -3 \end{bmatrix}_1,$$

which gives the basis DSC vectors as $\boldsymbol{a} = \frac{1}{162}[11\,\overline{13}\,14]_1$, $\boldsymbol{b} = \frac{1}{162}[19\,7\,\overline{20}]_1$ and $\boldsymbol{c} = \frac{1}{54}[\overline{2}\overline{5}\overline{5}]_1$.

Figs 9*a* and 9*b* show, for GBD A, experimental images and matching theoretical images computed for $\boldsymbol{b}_A = \frac{1}{162}[11\,\overline{13}\,14]_1$. The experimental image in Fig. 9*b* proved to be a particularly definitive image for eliminating a large number of possible Burgers vectors for GBD A. It can be seen that in this experimental image the contrast of GBD A is very weak with weak dark intensity below the line of the GBD, whereas many of the possible Burgers vectors gave images with stronger contrast with strong light intensity above the line of the GBD, as shown by the examples of the non-matching theoretical images in Figs 9*c–e*.

Figs 10*a* and 10*b* show experimental images and matching theoretical images for the GBD segments B and C, respectively, with $\boldsymbol{b}_B = \frac{1}{162}[19\,7\,\overline{20}]_1$ and $\boldsymbol{b}_C = \frac{1}{54}[\overline{2}\overline{5}\overline{5}]_1$. In the experimental image shown in Fig. 11*a*, the GBD segment C shows weak contrast throughout the thickness of the foil and is another example of an image which enabled many of the possible Burgers vectors to be eliminated in the identification procedure. For example, the theoretical image in Fig. 11*b*, corresponding to $\boldsymbol{b}_C = \frac{1}{54}[\overline{2}\overline{5}\overline{5}]_1$, is a good match in that it shows the type of weak contrast observed at the line

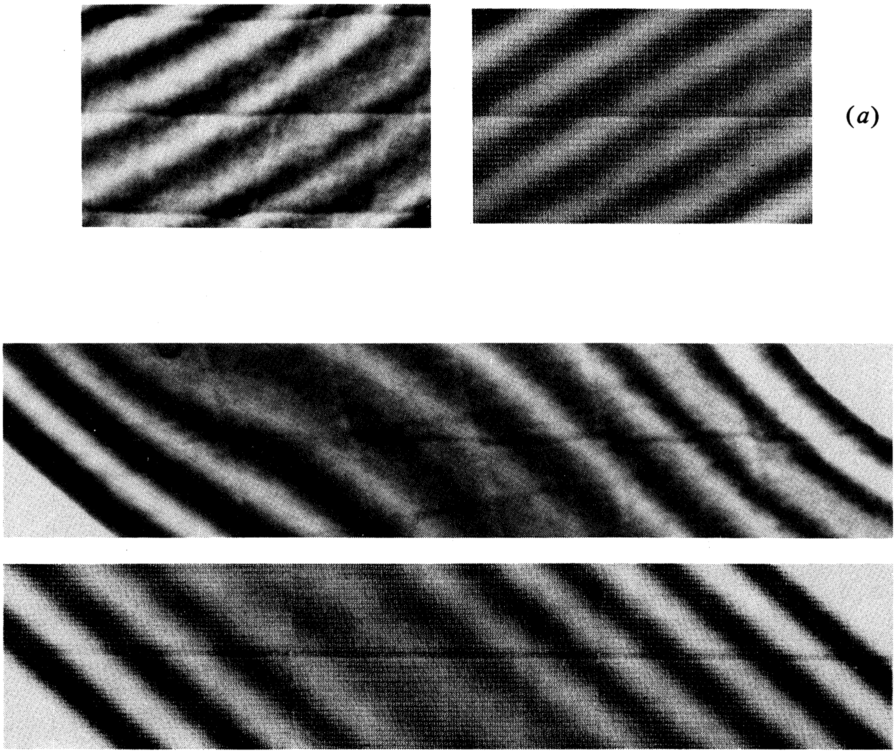

(a)

(b)

Fig. 10. Matching experimental and theoretical images for the secondary GBDs (*a*) B and (*b*) C in the network of Fig. 8. The boundary normal, foil thickness and foil normal are given in Fig. 9 and the GBD line directions $\boldsymbol{l}$ are $[\overline{43}\,\overline{28}\,13]_1$ for B and $[\overline{13}\,11\,\overline{18}]_1$ for C. The diffraction parameters for the experimental images and the theoretical images computed for $\boldsymbol{b}_B = \frac{1}{162}[19\,7\,\overline{20}]_1$ and $\boldsymbol{b}_C = \frac{1}{54}[\overline{2}\overline{5}\overline{5}]_1$ are:

Fig.	$\boldsymbol{g}$	$\boldsymbol{B}$	w	Fig.	$\boldsymbol{g}$	$\boldsymbol{B}$	w
(*a*)	$11\overline{1}_1$	$[\overline{1}32]_1$	$0{\cdot}13_1$	(*b*)	$\overline{1}1\overline{1}_1$	$[\overline{2}57]_1$	$0{\cdot}23_1$
	200_2	$[012]_2$	$0{\cdot}10_2$		$\overline{2}00_2$	$[0\,1\,12]_2$	$0{\cdot}23_2$

of the GBD in the experimental image throughout the entire foil thickness, with this contrast virtually disappearing near the bottom surface of the foil (left-hand side of image). However, the other two theoretical images (*c*) and (*d*), which were computed for Burgers vectors having given theoretical images that matched experimental images for other diffracting conditions, are mismatches in this case as they show strong contrast throughout the entire thickness of the foil, and therefore can be eliminated.

In summary, the image matching technique identified the Burgers vectors of the secondary GBD network in this near $\Sigma 81$a boundary as $\boldsymbol{b}_A = \boldsymbol{a} = \frac{1}{162}[11\,\overline{13}\,14]_1$, $\boldsymbol{b}_B = \boldsymbol{b} = \frac{1}{162}[19\,7\,\overline{20}]_1$ and $\boldsymbol{b}_C = \boldsymbol{c} = \frac{1}{54}[\overline{2}\overline{5}\overline{5}]_1$.

5. Discussion

The present results have confirmed, for a range of near CSL orientations, that, in accordance with the secondary GBD model of high angle boundaries as discussed

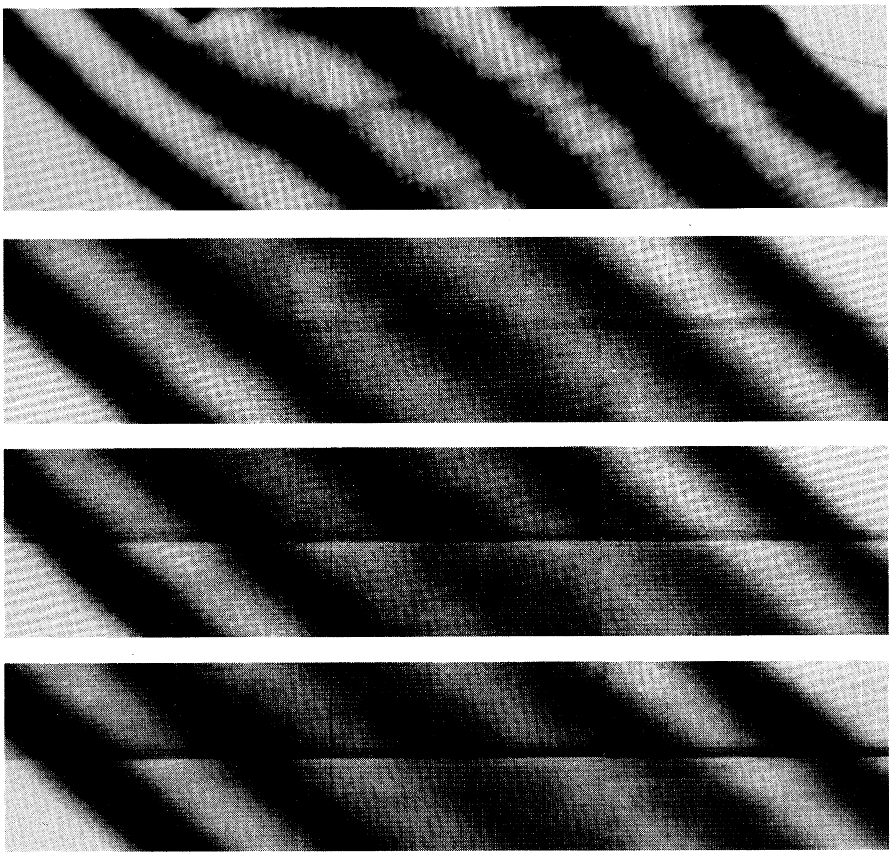

(a)

(b)

(c)

(d)

Fig. 11. Matching experimental and theoretical images (*a*) and (*b*) for GBD C of Fig. 8 for $\boldsymbol{b}_C = \frac{1}{54}[\bar{2}\bar{5}\bar{5}]_1$. The GBD line direction is $[\overline{13}\,11\,\overline{18}]_1$ and the boundary normal, foil thickness and foil normal are given in Fig. 9. The diffraction parameters are:

$\boldsymbol{g}$	$\boldsymbol{B}$	w
$02\bar{2}_1$	$[\bar{1}\,11\,11]_1$	$0{\cdot}45_1$
$\bar{2}20_2$	$[115]_2$	$0{\cdot}10_2$

The additional theoretical images (*c*) and (*d*) were computed for the same diffraction parmeters with $\boldsymbol{b}_C = \frac{1}{162}[\overline{17}\,\bar{2}\,\overline{29}]_1$, (*c*); and $\boldsymbol{b}_C = \frac{1}{162}[\overline{23}\,\overline{17}\,\overline{44}]_1$, (*d*).

in Section 2, the Burgers vectors of the secondary GBDs are vectors of the DSC lattice of the appropriate CSL. Although in principle more than three independent arrays of secondary GBDs could be involved in accommodating the departure of the misorientation across a high angle boundary from an exact CSL orientation [see equation (2) of Section 2] it has been found, for the cases discussed in detail here and for many others investigated, that only three independent arrays of GBDs occur in the secondary GBD networks. In many cases additional segments are present in secondary GBD arrays, but as has been shown here for the near $\Sigma 9$, $\Sigma 27$a and $\Sigma 27$b boundaries, they do not represent independent arrays of GBDs, since they arise from energy lowering reactions between pairs of GBDs in the three independent sets.

In all cases studied some of the segments in the secondary GBD networks cross one another without interaction, resulting in four-fold nodes. This arises because in some cases reactions would be energetically neutral on a b^2 criterion (for example, a reaction between GBDs A and D for the near $\Sigma 9$ boundary, and between GBDs B and D for the near $\Sigma 27$a boundary), while in other cases reactions do not occur because of the large difference in the magnitudes of the Burgers vectors and hence the line tensions of the crossing GBD segments (for example, the GBDs A and D in the near $\Sigma 27$a boundary and A and C in the near $\Sigma 27$b boundary).

For the different types of near CSL boundary examined, the Burgers vectors for most of the secondary GBDs were found to be the basis vectors of the appropriate DSC lattice. The fact that the Burgers vectors are predominantly basis vectors is to be expected, because these Burgers vectors minimize the overall self-energy of the arrays of secondary GBDs required in the boundary to accommodate the departure of the misorientation from a particular CSL orientation. However, this self-energy argument cannot be the sole factor determining the values of the DSC Burgers vectors of secondary GBDs, because on occasions Burgers vectors are found for segments of secondary GBD networks which are not basis DSC vectors, but are simple linear combinations of basis vectors. Two examples here are segments A in the near $\Sigma 27$a and near $\Sigma 27$b boundaries which have the Burgers vectors $\frac{1}{6}[\bar{1}12]_1$ and $\frac{1}{54}[1\,\overline{19}\,\bar{4}]_1$ respectively. An additional factor may be the energy of the steps associated with the secondary GBDs (King and Smith 1980).

Because the magnitudes of the basis DSC vectors decrease with increasing Σ value, the intensity of the diffraction contrast of the secondary GBDs with these basis DSC Burgers vectors also decreases as the Σ value increases. For example, the contrast level associated with the secondary GBDs in the near $\Sigma 81$a boundary is much less than that associated with the secondary GBDs in the near $\Sigma 9$ boundary (compare, for example, Fig. 8 with Fig. 1). This decrease in the intensity of diffraction contrast did not impair the identification of the Burgers vectors by image matching for Σ values up to $\Sigma 81$, in the present work, but identification of smaller basis vectors, associated with appreciably higher Σ values, could present difficulties.

Acknowledgments

We are indebted to our colleagues Dr A. K. Head and Dr P. Humble for adapting the image matching programs for use on a 'Corona' personal computer.

References

Barry, D. E., and Mahajan, S. (1971). *Philos. Mag.* **23**, 727.
Bollmann, W. (1967). *Philos. Mag.* **16**, 363; 383.
Bollmann, W., Michaut, B., and Sainfort, G. (1972). *Phys. Status Solidi (a)* **13**, 637.
Clarebrough, L. M. (1974). *Philos. Mag.* **30**, 1295.
Clarebrough, L. M., and Forwood, C. T. (1980*a*). *Phys. Status Solidi (a)* **58**, 597.
Clarebrough, L. M., and Forwood, C. T. (1980*b*). *Phys. Status Solidi (a)* **59**, 263.
Clark, W. A. T., and Smith, D. A. (1978). *Philos. Mag.* **38**, 367.
Forwood, C. T., and Clarebrough, L. M. (1983). *Philos. Mag.* **47**, L35.
Forwood, C. T., and Clarebrough, L. M. (1984). *Acta Metall.* **32**, 757.

Forwood, C. T., and Clarebrough, L. M. (1985). *Philos. Mag.* A **51**, 589.
Forwood, C. T., and Humble, P. (1975). *Philos. Mag.* **31**, 1025.
Frank, F. C. (1949). *Physica* **15**, 131.
Frank, F. C. (1950). 'Plastic Deformation of Crystalline Solids', p. 150 (Carnegie Inst. Technology: Pittsburgh).
Grimmer, H. (1974). *Scr. Metall.* **8**, 1221.
Grimmer, H., Bollmann, W., and Warrington, D. H. (1974). *Acta Crystallogr.* A **30**, 197.
Head, A. K., Humble, P., Clarebrough, L. M., Morton, A. J., and Forwood, C. T. (1973). 'Computed Electron Micrographs and Defect Identification' (North-Holland: Amsterdam).
Humble, P., and Forwood, C. T. (1975). *Philos. Mag.* **31**, 1011.
King, A. H., and Smith, D. A. (1980). *Acta Crystallogr.* A **36**, 335.
Neighbours, J. R., and Smith, C. S. (1954). *Acta Metall.* **2**, 591.
Pond, R. C., and Vitek, V. (1977). *Proc. R. Soc. London* A **357**, 453.
Pumphrey, P. H. (1975). *Phys. Status Solidi (a)* **28**, 545.
Tucker, M. O. (1969). *Philos. Mag.* **19**, 1141.

Manuscript received 16 January, accepted 27 March 1985